Silicon high-speed binary phase-shift keying modulator with a single-drive push–pull high-speed traveling wave electrode

Jinting Wang,[1] Linjie Zhou,[1,*] Haike Zhu,[1] Rui Yang,[1] Yanyang Zhou,[1] Lei Liu,[2] Tao Wang,[2] and Jianping Chen[1]

[1]State Key Laboratory of Advanced Optical Communication Systems and Networks, Department of Electronic Engineering, Shanghai Jiao Tong University, Shanghai 200240, China
[2]Transmission Technology Research Department, Huawei Technologies Co. Ltd., Shenzhen 518129, China
*Corresponding author: ljzhou@sjtu.edu.cn

Received November 28, 2014; revised February 12, 2015; accepted February 12, 2015; posted February 13, 2015 (Doc. ID 228707); published April 6, 2015

We demonstrate binary phase shift keying (BPSK) modulation using a silicon Mach–Zehnder modulator with a π-phase-shift voltage (V_π) of –4.5 V. The single-drive push–pull traveling wave electrode has been optimized using numerical simulations with a 3 dB electro-optic bandwidth of 35 GHz. The 32 Gb/s BPSK constellation diagram is measured with an error vector magnitude of 18.9%. © 2015 Chinese Laser Press

OCIS codes: (230.3120) Integrated optics devices; (250.3140) Integrated optoelectronic circuits; (250.7360) Waveguide modulators.
http://dx.doi.org/10.1364/PRJ.3.000058

With the number of processing cores increasing in central processing units, the electrical interconnects gradually become the bottleneck for the further improvement of computing performances due to their large delay, low bandwidth, and high power consumption [1]. Optical interconnects based on silicon photonics have been regarded as a promising solution to this problem. Silicon optical modulators, which are used to encode electrical signals onto optical beams, are a major workhorse in optical interconnects [2,3]. Till now, the reported high-speed silicon modulators are dominantly based on two optical structures: the Mach–Zehnder interferometer (MZI) [4–7] and the resonant cavity [8–10]. Silicon modulators based on microrings and microdisks have the merits of small size, low modulation power, and high modulation speed of up to 50 Gb/s [11]. However, they also suffer from certain limitations, such as narrow optical bandwidth and high temperature sensitivity, which greatly limit their practical applications. Silicon modulators based on MZIs, on the other hand, have broad optical bandwidth and high tolerance to temperature fluctuations. Modulation speeds up to 70 Gb/s have also been recently demonstrated in MZI modulators (MZMs) integrated with reverse-biased $p-n$ junctions [12]. A higher modulation speed can be expected by reducing the radio-frequency (RF) loss of transmission lines [13], as the modulation bandwidth is partially limited by the attenuation of RF drive signals.

Advanced modulation formats are necessary to increase the aggregation data rate within a limited spectral bandwidth. As the basis for advanced modulation formats, binary phase-shift keying (BPSK) modulation based on a silicon MZM has been reported [14]. In their design, separate traveling wave electrodes (TWEs) on the two MZI arms are used, requiring differential RF signals [15].

In this paper, we demonstrate a silicon BPSK modulator using a MZI structure driven by a single-drive push–pull TWE. The TWE has been optimized with numerical simulations. 32 Gb/s BPSK modulation is achieved with an error vector magnitude (EVM) of 18.9%.

To design a high-speed modulator, we consider three main factors that determine the modulation bandwidth. First of all, the characteristic impedance (Z_0) of the TWE needs to approach 50 Ω in order to avoid RF signal backreflection from the ends of the TWE. Second, the RF attenuation of the TWE should be small, since the electro-optic (EO) 3 dB bandwidth is related to the RF electro-electro (EE) 6.4 dB bandwidth [16]. Third, the electrical and optical waves need to be synchronized to provide the highest modulation efficiency [17]. For a lossless modulator with impedance-matched load and generator, its EO 3 dB bandwidth is determined by the velocity mismatch between the RF and optical signals and is given by [18]

$$f_{3\,\mathrm{dB}} = \frac{0.18}{(n_{\mathrm{eff}} - n_0)l}, \tag{1}$$

where l is the electrode length, n_{eff} is the microwave refractive index, and n_0 is the group refractive index of the waveguide optical mode. To increase the modulation bandwidth, n_{eff} needs to approach n_0.

Figure 1(a) shows the schematic structure of our BPSK modulator consisting of an asymmetric MZI integrated with a single-drive TWE. We adopt the asymmetric MZI structure because the bias point (π-phase difference) needed for BPSK can be conveniently obtained by tuning the input laser wavelength. In principle, a symmetric MZI structure can be used to provide a large optical bandwidth, but a phase shifter (e.g., based on a microheater) is also needed to set the bias point.

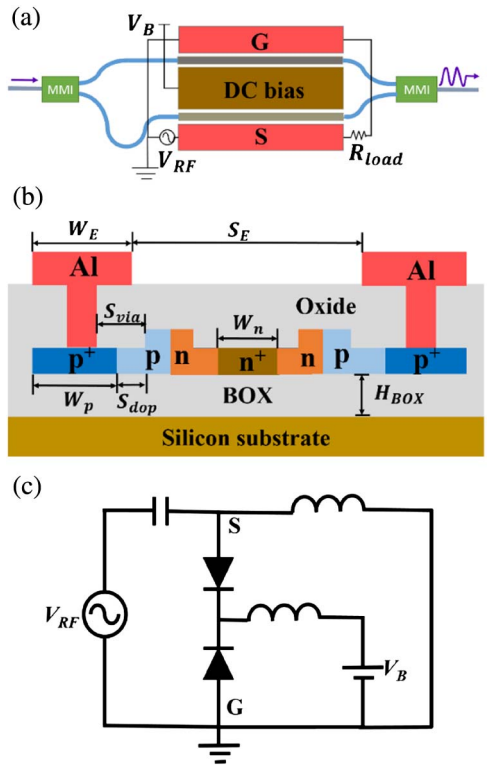

Fig. 1. (a) Schematic structure of the BSPK modulator. (b) Cross section of modulation arms showing the single-drive TWE. (c) Equivalent circuit model of the TWE.

The modulation arm length is 3 mm. Figure 1(b) shows the cross section of the MZM. Six key parameters related to the TWE need to be optimized, including the width of the metal lines W_E, the separation of the metal lines S_E, the width of the p^+ doping region W_p, the width of the n^+ doping region W_n, the separation of the via from waveguide S_{via}, and the separation of p^+/n^+ doping from waveguide S_{dop}. The silicon waveguide has a width of 500 nm and a height of 220 nm with a slab thickness of 60 nm. The separation between MZI arms is 120 μm. The p and n doping concentrations in the $p-n$ junctions are $\sim 4\times10^{17}$ and $\sim 1\times10^{18}$ cm^{-3}, respectively. The n^+ doping region in the center of the MZI has a doping concentration of $\sim 10^{20}$ cm^{-3}, connected with a DC bias terminal. The two p^+ doping regions at the outer sides of the MZI have a doping concentration of $\sim 10^{20}$ cm^{-3}, connected with the RF signal (S) and ground (G) terminals. The equivalent circuit model of the single-drive TWE is shown in Fig. 1(c). The two $p-n$ junctions (one for each arm) are back-to-back connected. The RF signal V_{RF} is applied between S and G terminals. A common DC bias V_B is applied to the middle n^+ doping region. Hence, the voltages dropped on the two junctions are $-V_B + V_{\text{RF}}/2$ and $-V_B - V_{\text{RF}}/2$, respectively, forming a push–pull fashion with only a single RF input.

The large $p-n$ junction capacitance makes it difficult to design a high-speed TWE to meet the three criteria mentioned above. The single-drive TWE design can effectively reduce the total capacitance to half, as the two junction capacitors in the two arms are connected in series. The push–pull scheme also reduces the modulation-induced frequency chirp [19].

In our first version of design, the TWE parameters are chosen according to the literature reports [13,15–19] and are listed in Table 1 (the device is denoted as MZI-1). Figure 2 shows the simulated EE-S21, Z_0, and n_{eff} responses using the COMSOL RF module. The EO-S21 response is calculated from an equivalent circuit model [18]. The EE 3 dB bandwidth is 10 GHz, and the EO 3 dB bandwidth is 25 GHz. n_{eff} approaches 3.2 at high RF frequencies. Z_0 is close to 50 Ω at low frequencies but tends to increase with frequency. To further improve the modulator performance, we need to reduce RF attenuation and increase n_{eff} with all TWE parameters taken into consideration during optimization. It is impossible to scan all parameters simultaneously, and therefore we start from MZI-1 and vary only one TWE parameter at a time to simulate the change trend of RF attenuation, Z_0, and n_{eff}. It should be noted that in S_E scan, S_{via} is revised to 18 μm in order to ensure the metal lines are always connected with the contact holes. From the change trend and taking into consideration the three factors that affect the TWE performance, we can further improve the modulation bandwidth.

Table 1. TWE Parameters of BPSK Modulators

Name	W_E(μm)	S_E(μm)	W_p(μm)	W_n(μm)	S_{via}(μm)	S_{dop}(μm)
MZI-1	25	16	20	12	4.5	0.8
MZI-2	60	50	20.7	16.2	16.7	0.5

Figure 3 shows the simulation results. The RF frequency is set at 28 GHz, and the $p-n$ junction bias voltage is set at –4 V. It can be seen that S_E has the most significant influence on all three factors, and it is the only variable that can increase n_{eff}. Yet there is a trade-off between RF attenuation and velocity match. We choose a larger S_E to let n_{eff} approach n_0 at the cost of a higher RF attenuation. To compensate for the RF loss, W_E is increased and S_{dop} is decreased as shown in Figs. 3(a) and 3(e). Increasing W_E also helps to counteract the increase of Z_0 after choosing a larger S_E. Given the TWE geometry, the increasing S_E requires simultaneously

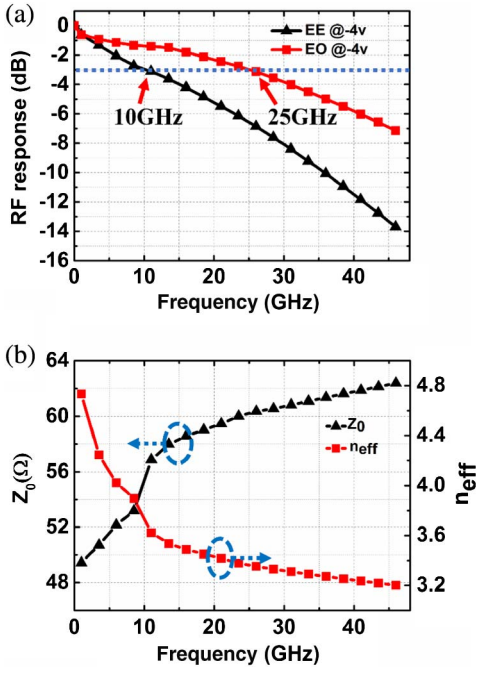

Fig. 2. Simulation results of MZI-1. (a) EE and EO S21 responses. (b) Z_0 and n_{eff} versus RF frequency.

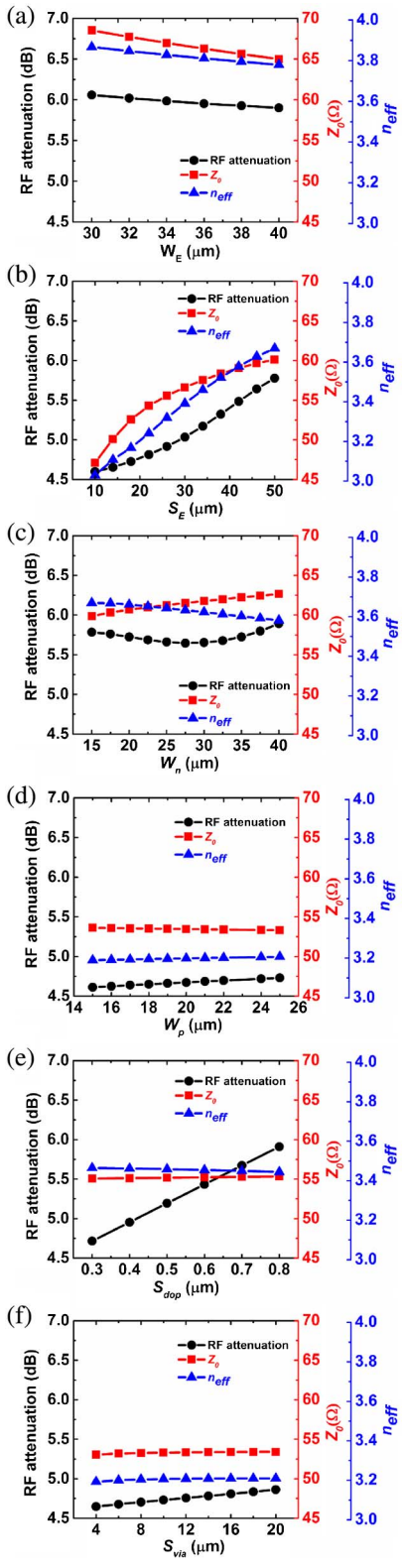

Fig. 3. Effects of various TWE parameters: (a) W_E, (b) S_E, (c) W_n, (d) W_p, (e) S_{dop}, and (f) S_{via} on RF attenuation, Z_0, and n_{eff}.

increased S_{via} and W_p to guarantee good metal contact. As shown in Figs. 3(d) and 3(f), S_{via} and W_p have little impact on TWE performance, and hence it is safe to increase them. W_n is finally fine-tuned to achieve a small RF loss and matched impendence.

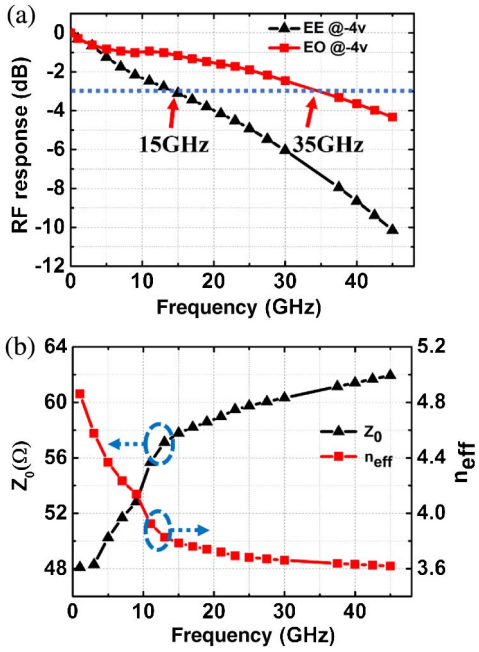

Fig. 4. Simulation results of MZI-2. (a) EE and EO S21 responses. (b) Z_0 and n_{eff} versus RF frequency.

The final optimized parameters are shown in Table 1 (MZI-2). Figure 4 shows the frequency responses of S21, Z_0, and n_{eff} for the improved design. Compared with the original one, the EE 3 dB bandwidth is increased to 15 GHz, and n_{eff} is increased to 3.6 at high RF frequencies, closer to the optical waveguide group index of 4.023. The EO 3 dB bandwidth is hence improved to 35 GHz. It should be noted that the thickness of the buried oxide (BOX) layer H_{BOX} also affects the modulator EO bandwidth. However, given that H_{BOX} is determined by the silicon-on-insulator (SOI) wafers and thereby cannot be freely designed on the mask level like the other parameters, we did not specifically optimize this parameter.

Our device was fabricated at the Institute of Microelectronics (IME) Singapore using complementary metal-oxide-semiconductor (CMOS) compatible processes. The starting material is a SOI wafer with a 220 nm thick top silicon layer and a 2 μm thick BOX layer. 248 nm deep ultraviolet photolithography was used to define the waveguide patterns, followed by anisotropic dry etch of silicon. The p^+, p, n, and n^+ doping was obtained by ion implantation followed by rapid thermal annealing at 1030°C for 5 s [16]. Silicon dioxide was then deposited and contact holes were etched. Finally aluminum was deposited and etched to form the metal connection.

Figure 5 shows the measured optical transmission spectra when the applied voltage on the lower arm is varied from 0 to −6 V. The insertion loss is about 15 dB, including 4 dB/facet coupling loss, 6 dB waveguide loss, and 1 dB loss from the multimode interferometers that compose the MZI. The interference notch is shifted by half a free spectral range under a reverse voltage of 4.5 V, which indicates the modulation efficiency is $V_\pi L = 1.35\ \text{V}\cdot\text{cm}$.

We measured the EE S-parameters of the TWE from DC to 26 GHz by using a vector network analyzer (Agilent N5247A) under various bias voltages, as shown in Fig. 6. The measured 3 dB bandwidth reaches 15.5 GHz when the MZM is biased at

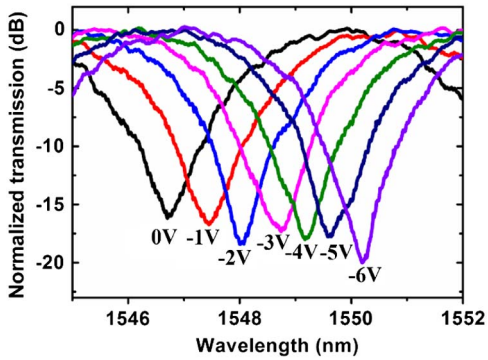

Fig. 5. Measured optical transmission spectra under various bias voltages.

−4 V, matching with the simulation result in Fig. 4(a). S11 is less than −15 dB for the full measured frequency range, implying good impendence match.

We then measured the eye diagrams of the BPSK modulated signals. A 32 Gb/s pulse pattern generator was used to generate the pseudo-random binary sequence RF drive signals with a $2^{23} - 1$ pattern length. The peak-to-peak voltage (V_{pp}) was ~6 V after amplification. The RF signal was applied to the TWE through a 40 GHz GS probe. The other end of the TWE was terminated with a 50 Ω resistor by using another SG probe. −3 V DC bias voltage was applied to the device through a print circuit board wire-bonded with the chip. The input laser light with 12 dBm optical power was coupled to the modulator. The output light with around −10 dBm optical power was amplified by an erbium-doped fiber amplifier followed by a 1 nm bandwidth optical filter to compensate for the device insertion loss. The amplified optical signal was then fed into a digital oscilloscope for eye-diagram measurement or to an optical modulation analyzer for constellation diagram

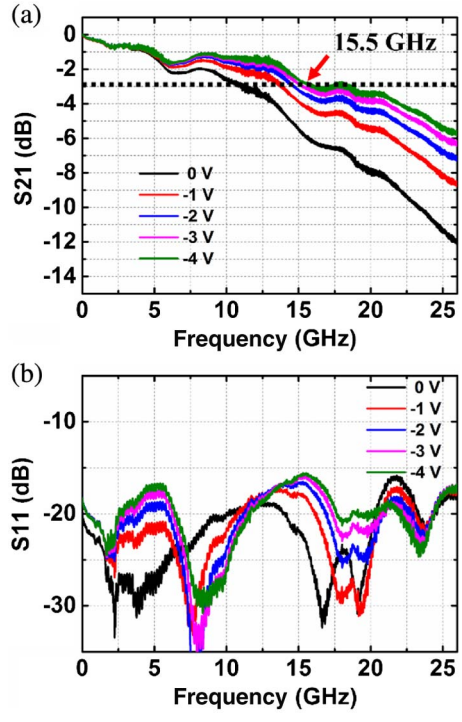

Fig. 6. Measured (a) S21 and (b) S11 responses of MZI-2 with DC bias voltage varying from 0 to −4 V.

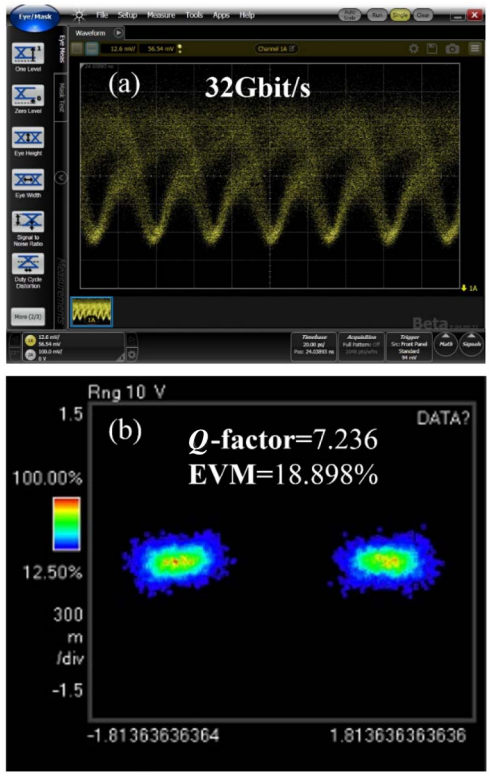

Fig. 7. (a) Measured BPSK signal eye diagram. (b) Measured BPSK constellation diagram. The signal data rate is 32 Gb/s.

measurement. Figure 7 shows the measured results. The constellation diagram measurement suggests the BPSK signal *Q*-factor is 7.2 and EVM is 18.9%.

In conclusion, we have demonstrated a 32 Gb/s BPSK modulator with an optimized 3 mm long single-drive push–pull TWE. Numerical simulation was carried out to analyze the effect of various TWE geometric parameters on the TWE performance. The measured modulation efficiency is $V_\pi L = 1.35$ V · cm. S-parameter characterization reveals that the 3 dB EE bandwidth of the TWE is 15 GHz, corresponding to 35 GHz EO bandwidth of the modulator. The 32 Gb/s BPSK constellation diagram was also measured with an EVM of 18.9%.

ACKNOWLEDGMENTS

This work was supported in part by the National 973 Program of China (2011CB301700), the National 863 Program of China (2013AA014402), the National Natural Science Foundation of China (NSFC) (61127016, 61107041, and 61422508), and the Specialized Research Fund for the Doctoral Program of Higher Education of Ministry of Education (20130073130005). We also acknowledge IME Singapore for device fabrication.

REFERENCES

1. L. Yang and J. Ding, "High-speed silicon Mach-Zehnder optical modulator with large optical bandwidth," IEEE J. Lightwave Technol. **32**, 966–970 (2014).
2. X. Li, X. Feng, K. Cui, F. Liu, and Y. Huang, "Integrated silicon modulator based on microring array assisted MZI," Opt. Express **22**, 10550–10558 (2014).
3. G. T. Reed, G. Mashanovich, F. Y. Gardes, and D. J. Thomson, "Silicon optical modulators," Nat. Photonics **4**, 518–526 (2010).

4. X. Xiao, H. Xu, X. Li, Z. Li, T. Chu, Y. Yu, and J. Yu, "High-speed, low-loss silicon Mach-Zehnder modulators with doping optimization," Opt. Express **21**, 4116–4125 (2013).
5. D. Marris-Morini, L. Vivien, J. M. Fédéli, E. Cassan, P. Lyan, and S. Laval, "Low loss and high speed silicon optical modulator based on a lateral carrier depletion structure," Opt. Express **16**, 334–339 (2008).
6. M. Ziebell, D. Marris-Morini, G. Rasigade, J. M. Fédéli, P. Crozat, E. Cassan, D. Bouville, and L. Vivien, "40 Gbit/s low-loss silicon optical modulator based on a pipin diode," Opt. Express **20**, 10591–10596 (2012).
7. T. Li, D. Wang, J. Zhang, Z. Zhou, F. Zhang, X. Wang, and H. Wu, "Demonstration of 6.25 Gbaud advanced modulation formats with subcarrier multiplexed technique on silicon Mach-Zehnder modulator," Opt. Express **22**, 19818–19823 (2014).
8. F. Y. Gardes, A. Brimont, P. Sanchis, G. Rasigade, D. Marris-Morini, L. O'Faolain, F. Dong, J. M. Fedeli, P. Dumon, L. Vivien, T. F. Krauss, G. T. Reed, and J. Martí, "High-speed modulation of a compact silicon ring resonator based on a reverse-biased pn diode," Opt. Express **17**, 21986–21991 (2009).
9. W. D. Sacher, W. M. J. Green, S. Assefa, T. Barwicz, H. Pan, S. M. Shank, Y. A. Vlasov, and J. K. S. Poon, "Coupling modulation of microrings at rates beyond the linewidth limit," Opt. Express **21**, 9722–9733 (2013).
10. A. Malacarne, F. Gambini, S. Faralli, J. Klamkin, and L. Potì, "30-Gbps silicon microring modulator for short- and medium-reach optical interconnects," in *Optical Fiber Communication Conference*, OSA Technical Digest (online) (Optical Society of America, 2014), paper Th2A.4.
11. T. Baba, S. Akiyama, M. Imai, N. Hirayama, H. Takahashi, Y. Noguchi, T. Horikawa, and T. Usuki, "50-Gb/s ring-resonator-based silicon modulator," Opt. Express **21**, 11869–11876 (2013).
12. H. Xu, X. Li, X. Xiao, P. Zhou, Z. Li, J. Yu, and Y. Yu, "High-speed silicon modulator with band equalization," Opt. Lett. **39**, 4839–4842 (2014).
13. J. Ding, H. Chen, L. Yang, L. Zhang, R. Ji, Y. Tian, W. Zhu, Y. Lu, P. Zhou, and R. Min, "Low-voltage, high-extinction-ratio, Mach-Zehnder silicon optical modulator for CMOS-compatible integration," Opt. Express **20**, 3209–3218 (2012).
14. T. Li, J. Zhang, H. Yi, W. Tan, Q. Long, Z. Zhou, X. Wang, and H. Wu, "Low-voltage, high speed, compact silicon modulator for BPSK modulation," Opt. Express **21**, 23410–23415 (2013).
15. H. Zhu, L. Zhou, L. Liu, T. Wang, Y. Zhou, J. Wang, Q. Wu, A. Xie, R. Yang, Z. Li, X. Li, and J. Chen, "Single-drive push-pull silicon Mach-Zehnder modulator for OOK and BPSK modulation," in *OptoElectronics and Communication Conference and Australian Conference on Optical Fibre Technology* (IEEE, 2014), pp. 174–175.
16. M. Streshinsky, R. Ding, Y. Liu, A. Novack, Y. Yang, Y. Ma, X. Tu, E. K. S. Chee, A. E. J. Lim, P. G. Lo, T. Baehr-Jones, and M. Hochberg, "Low power 50 Gb/s silicon traveling wave Mach-Zehnder modulator near 1300 nm," Opt. Express **21**, 30350–30357 (2013).
17. Y. Zhou, L. Zhou, X. Sun, and J. Chen, "Design of traveling wave electrode for high-speed silicon modulators," in *Asia Communications and Photonics Conference*, OSA Technical Digest (online) (Optical Society of America, 2012), paper AS3B.2.
18. H. Yu and W. Bogaerts, "An equivalent circuit model of the traveling wave electrode for carrier-depletion-based silicon optical modulators," IEEE J. Lightwave Technol. **30**, 1602–1609 (2012).
19. P. Dong, L. Chen, and Y. Chen, "High-speed low-voltage single-drive push-pull silicon Mach-Zehnder modulators," Opt. Express **20**, 6163–6169 (2012).